Role of Texture and Microstructural Developments in the Forming Limit Diagrams of Family of Interstitial Free Steels

Basavaraj H. Vadavadagi, H.V. Bhujle, and Rajesh Kisni Khatirkar

Forming limit diagrams (FLDs) are widely used in sheet metal industries to assess formability. These are graphical representations of major and minor strains on a 2-D plot separating safe and unsafe regions. Limiting strains were measured by digital image correlation (DIC) technique. In the present work, microstructure evolution and forming behavior of family of interstitial free steels: interstitial free (IF) and interstitial free-high strength (IF-HS) grades have been investigated. Both experimental and finite element (FE) simulated FLDs indicated higher formability for IF steel. Microstructural developments affect forming limits and influence forming limit diagrams. Evolving microstructure during forming was studied by texture developments using x-ray diffraction (XRD) and in grain average misorientation developments using electron backscattered diffraction (EBSD) techniques as a function of strain and strain paths. Estimated microstructural parameters revealed that the enhanced formability of IF steel was due to the presence of strong γ-fiber (ND//$<111>$) recrystallization texture and corresponding absence of θ-fiber (ND//$<100>$). On the contrary, IF-HS steel showed the abundant θ-fiber component and hence decreased formability.

Basavaraj H. Vadavadagi and **H.V. Bhujle**, S.D.M. College of Engineering & Technology, Dhavalagiri, Dharwad, Karanataka 580002, India; and **Rajesh Kisni Khatirkar**, Visvesvaraya National Institute of Technology (VNIT), South Ambazari Road, Nagpur, Maharashtra 440010, India. Contact e-mail: vbasavaraj99@gmail.com.

Graphical Abstract
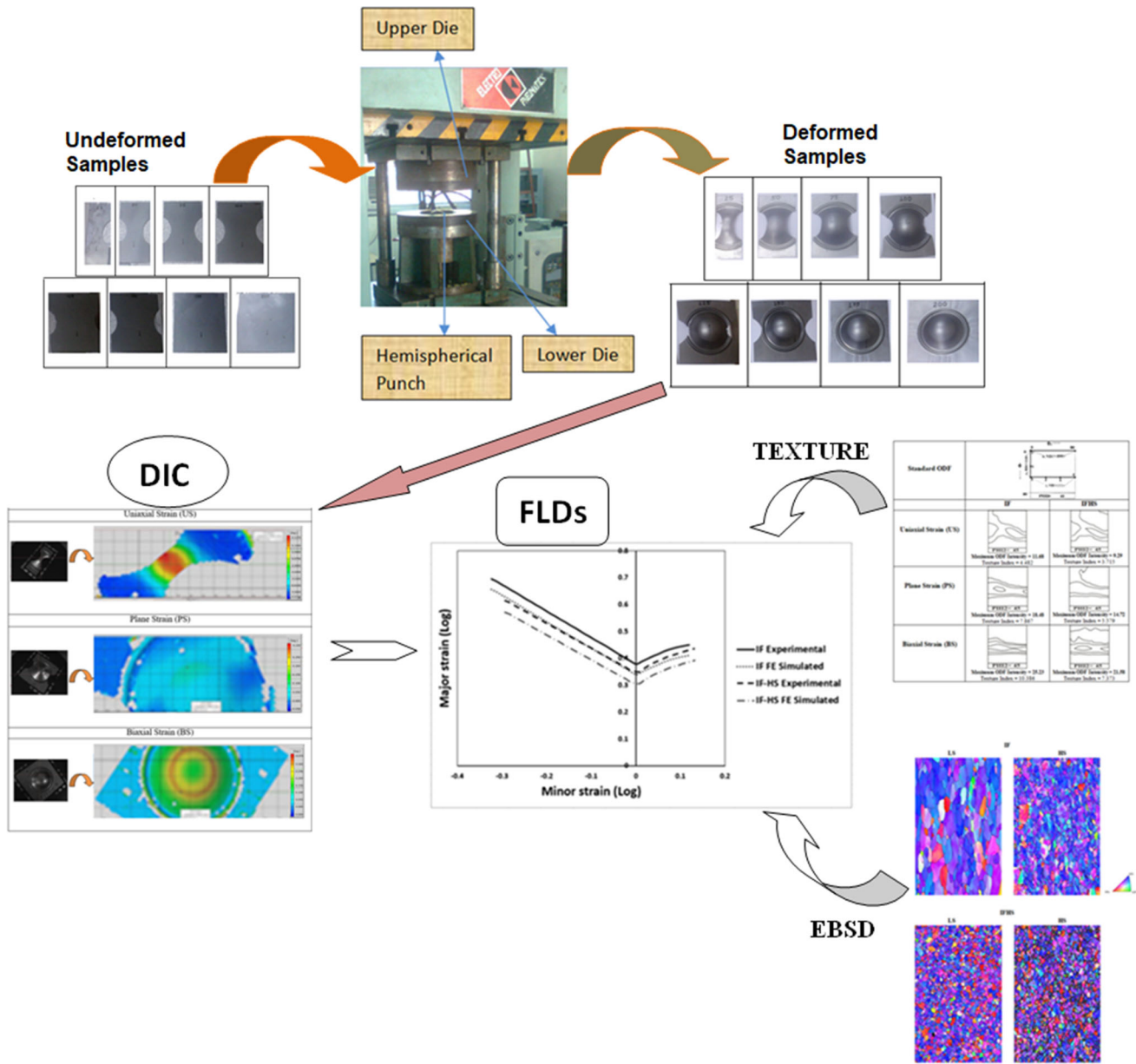
1. Introduction

Forming limit diagrams (FLDs) decide formability of a sheet metal (Ref 1-3). Basically, formability determines the ability of a metallic material to be shaped into final products before fracture. Strain-based FLDs are more common as compared to the stress-based FLDs. Forming limit diagram represents a plot of logarithm of major limit strains and minor limit strains separated by unsafe and safe zones. Instability in the material or diffused necking is usually observed in failure zones. Generally, FLDs are constructed either by conducting experiments or by numerical simulations. In-plane and out-of-plane are the two most significant techniques for determining experimental FLDs (Ref 4, 5). Recently, digital image correlation (DIC) technique is the most popular technique for accurate strain measurement employed for many applications in various industries. DIC being a full-field and especially non-contact type strain

Table 1 Chemical composition in wt% alloying elements of IF and IF-HS steels

	C	Mn	P	S	Si	Al	N	Ti	Nb	Fe
IF	0.0022	0.05	0.008	0.007	0.004	0.04	0.003	0.053	…	Balance
IFHS	0.0024	0.38	0.040	0.007	0.006	0.04	0.017	0.039	0.001	

Table 2 Mechanical properties of IF and IF-HS steels

Mechanical properties		IF steel	IF-HS steel
Yield strength, MPa		152	197
Ultimate tensile strength, MPa		295	372
Elongation, %		47	40
Strain hardening index, n	0°	0.33	0.26
	45°	0.28	0.23
	90°	0.31	0.24
	Avg.	0.3	0.25
r-values	0°	2.36	2.13
	45°	2.31	1.99
	90°	2.32	2.12
r-bar ($\bar{r}$)		2.34	2.08

measurement provides greater advantages. Various FLD determination methods using DIC technique are effectively practiced in recent past in the works of (Ref 6, 7). In this work, GOM^{TM}-ARGUS module has been extensively used during the measurement of limiting strains (both major and minor) and experimental FLDs were determined. Simulations of formability (Ref 8-11) assessment of metallic materials were carried out by many numerical tools including finite element (FE) techniques. Crystal plasticity models and different yield criteria are incorporated in advanced FE simulations (Ref 12-16) to simulate the behavior of materials. Failure assessment like onset of localized necking during different strain paths was predicted in (Ref 17, 18). Recently, a localized necking criterion which is based on micro-mechanical modeling (Ref 19, 20) has been developed for forming simulation. The various modeling approaches used for the determination of FLDs are critically reviewed in (Ref 21). Failure criteria like ductile fracture (Ref 22-24) and thickness gradient (Ref 25) were developed during FLD predictions.

Forming limit diagrams of metallic materials, on the other hand, depend on the properties of material like strain hardening exponent (n) and plastic anisotropy ratio ($\bar{r}$). Higher values of 'n' and $\bar{r}$ indicate higher formability, were investigated by (Ref 26) while studying the influence of material properties affecting forming limits diagrams. During deformation, the evolution of microstructure clearly demonstrated (Ref 27, 28) to be largely dependent on the strain path used and amount of strain. The microstructure and texture developments influence forming limit diagrams and hence formability was investigated by (Ref 29, 30). The role of texture development during FLD determination was studied by (Ref 29), while the works of (Ref 29-31) demonstrated the improved predictions of forming limit diagrams incorporating microstructural evolution. However, there exists limited literature on systematic investigations of microstructure and texture components influencing forming limit diagrams and hence formability in terms of developments in in-grain misorientations and texture developments, especially

in ferritic steels with body centered cubic crystal system. Quantification of microstructural evolution during formability assessment in ferritic steels with body centered cubic crystal system is uncharted. This being the motivation factor, our paper demonstrates a detailed study of microstructural developments, affecting forming limit diagrams as a function of strain and strain paths. In the present work, IF and IF-HS steel sheets were subjected to limiting dome height (LDH) experiments in order to estimate limiting strains in different strain paths; major and minor strain measurement was carried out by digital image correlation (DIC) technique and subsequently experimental FLDs were determined from the 2-D plots of major vs. minor strains with a demarcation line which separates safe and unsafe regions. Strain and stress-based FLDs were predicted from FE simulations using PAMSTAMP^{TM} software. Further, the effect of microstructure and texture developments in terms of γ-fiber and θ-fiber components on FLDs were analyzed by EBSD and XRD investigations.

2. Experimental Work and Finite Element Analysis

2.1 Materials and Methodology

Two grades of cold rolled and controlled annealed, IF and IF-HS steels were selected in this work. The initial thickness of both grades of steel was 0.8 mm. The chemical composition in weight percentage of both the steels chosen is given in Table 1. The base line mechanical properties of the two steels were determined by the tensile tests as per the standards ASTM E8M and ASTM E517 and the same were indicated in Table 2. Constant crosshead speed of 0.1 mm min^{-1} was maintained in both the tests. The normal anisotropy ($\bar{r}$) was estimated using Eq (1).

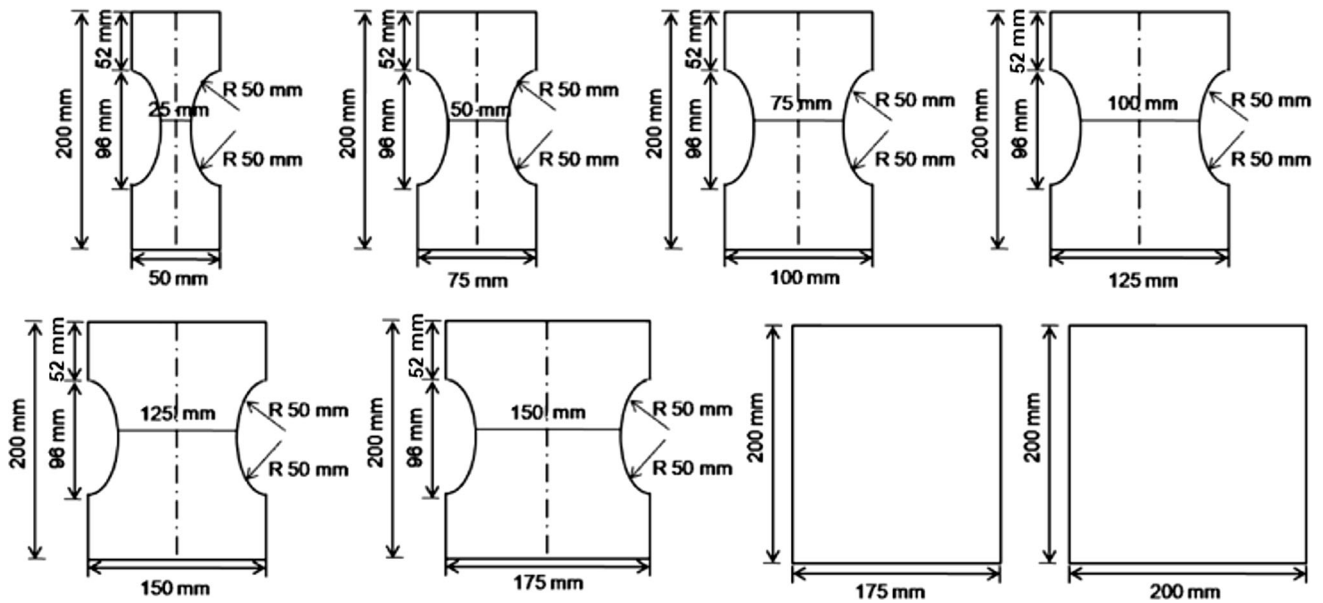$$\bar{r} = [r_0 + 2r_{45} + r_{90}]/4 \qquad \text{(Eq 1)}$$

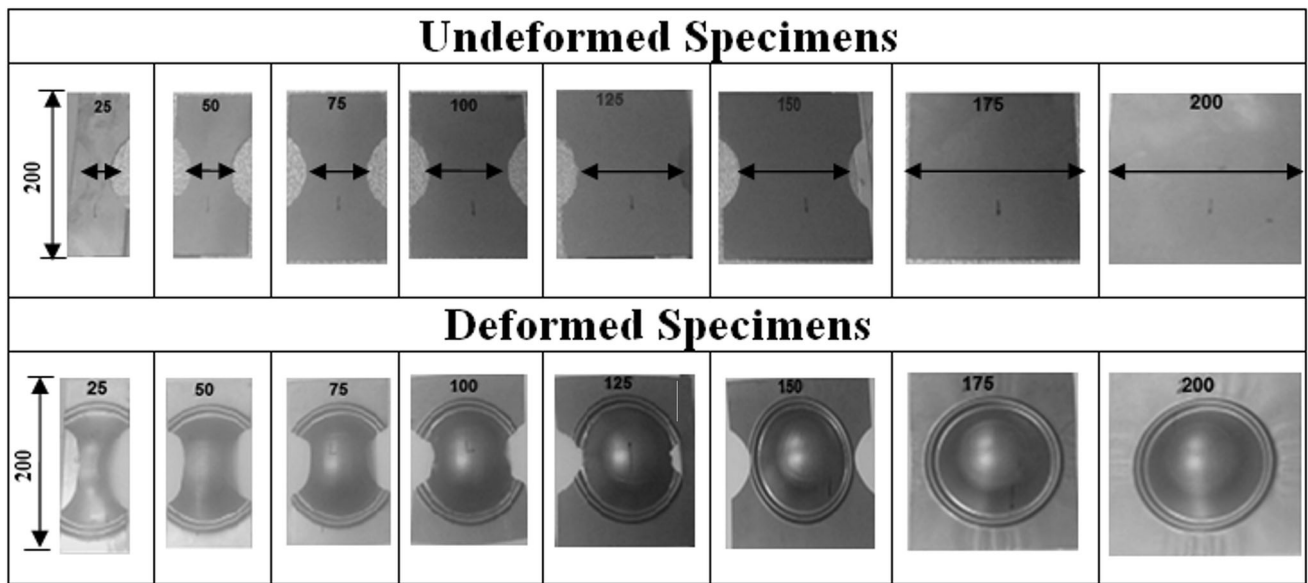**Fig. 1** Schematic of the specimens' geometry for LDH test

Fig. 2 Undeformed and deformed specimens of IF steel sheets. (All dimensions are in mm.)

where r_0, r_{45} and r_{90} are the plastic anisotropy ratios and the subscripts 0°, 45° and 90° indicate various directions of test samples w. r. t. rolling direction (RD) of the sample. In the present work, LDH experiments were conducted and experimental FLDs were determined using a servo-hydraulic double action forming press. In limiting dome height tests, rectangular specimens (hour-glass geometry) of length 200 mm varying widths, 25 to 200 mm at a step of 25 mm as shown in Fig. 1 were clamped firmly in the longitudinal direction and deformed over a 101.6 mm diameter hemispherical punch, thereby,

varying the lateral constraint. Such deformation controls the amount of lateral drawing-in and also changes the state of minor strain from positive state to a negative state. For each blank width, four specimens were tested to get maximum number of data points. For every sample, the height of the dome at maximum load (near fracture) and forming limit strains (major strain (ε_1) and minor strain (ε_2)) in the necked region were measured. Further these strains were plotted on a 2-D plot for constructing the forming limit diagrams. For the strain measurement, all eight undeformed samples of varying widths
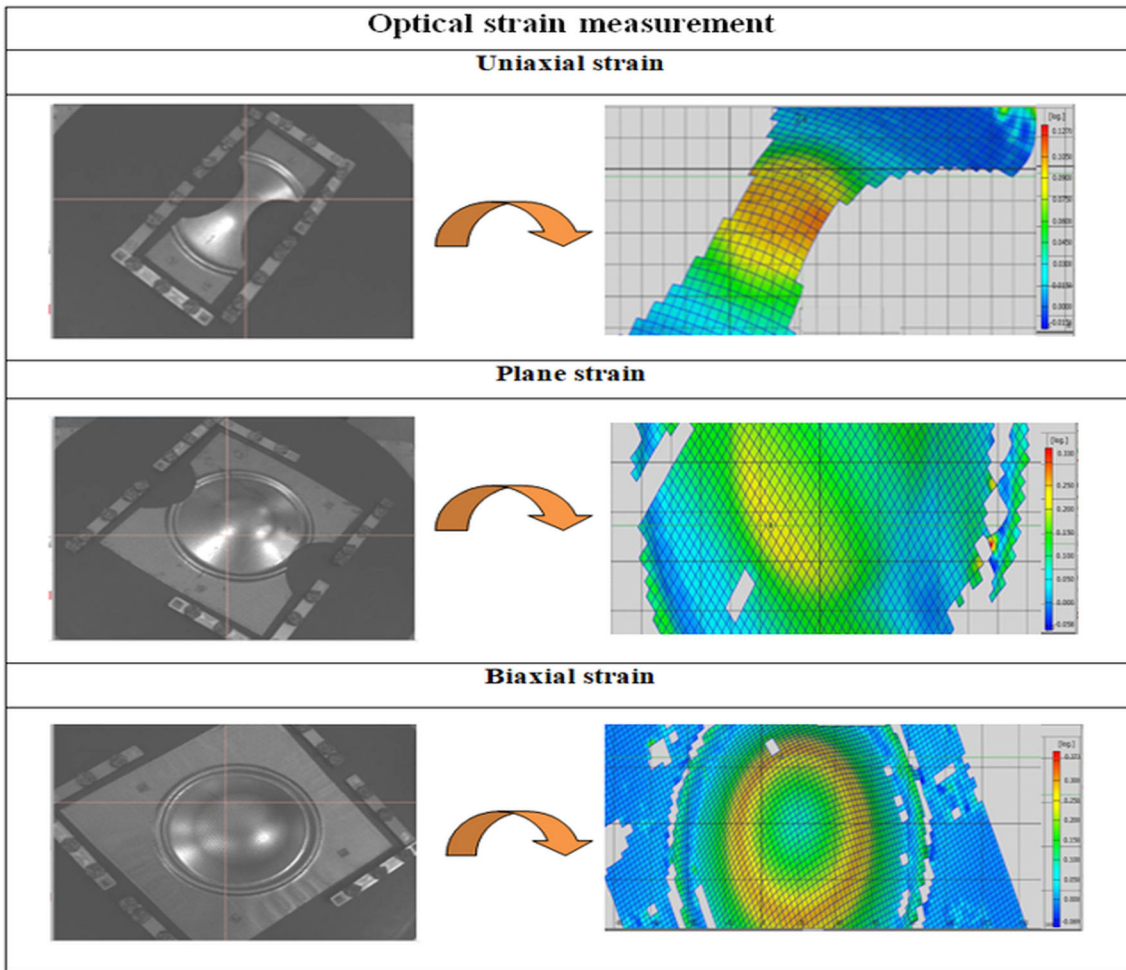
Fig. 3 Image acquisition by optical strain measurement system (GOM^{TM}) at different strain paths during measurement of major strain in IFHS steel sheets

were marked by circular dots of 1mm at a separation of 2.5 mm both in horizontal and vertical directions by screen print method. Varying width specimens were necessarily prepared to include different strain modes such as smaller widths for uniaxial strain (US), medium widths for plane strain (PS) and larger widths for biaxial strain (BS) specimens. Optical strain measuring system GOM^{TM} was extensively used for image acquisition of the specimens during pre- and post-deformation stages. After acquiring the images from undeformed specimens, LDH experiments were conducted. Figure 2 shows both undeformed and deformed specimens of IF steels. After LDH tests, once again image acquisition on the deformed specimens was completed. Finally, the major limit strains and minor limit strains were measured using digital image correlation. Figure 3 shows an example of optical strain measurement for IF-HS steel specimens. The thickness gradient criterion developed in (Ref 26) was used as a failure criterion in FLDs determination. Lastly, major strains and minor strains were plotted on a 2D plot and FLDs were drawn for both grades separating safe and failure zones. Fig. 4(a) and (b) represent FLDs of IF and IF-HS steel sheets, respectively, while Fig. 4(c) depicts superimposed FLDs of both steels.

3. Microstructural Characterization

The microstructural characterization of chosen areas on the deformed IF and IF-HS steels was carried out covering various strain levels and strain paths. Low ($\bar{\varepsilon} = 0.12 \sim 0.13$), intermediate ($\bar{\varepsilon} = 0.23 \sim 0.25$) and high ($\bar{\varepsilon} = 0.34 \sim 0.36$) strains were identified as various strain levels and strain paths such as uniaxial strain, plane strain and biaxial strain. Effective strains were estimated by Hill's 48 yield criterion (Ref 32) as indicated in Eq 2 ($\bar{\varepsilon}$, see Table 3)

$$\bar{\varepsilon} = \frac{1+\bar{r}}{(1+2\bar{r})^{1/2}} \left[\varepsilon_1^2 + \varepsilon_2^2 + \left(\frac{2\bar{r}}{1+\bar{r}} \right) \varepsilon_1 \varepsilon_2 \right]^{\frac{1}{2}} \qquad \text{(Eq 2)}$$

where $\bar{r}$ indicates plastic anisotropy and ε_1 and ε_2 referred as major and minor strains, respectively. For microstructural examination, electro-polishing was performed using Struers^{TM} Lectropol 3 at a temperature of -20°C and 11 volts DC for all samples as given in Table 3. The electrolyte used for electro-polishing consisted of a blend of ethanol and perchloric acid in the ratio 80:20. Bulk texture measurements were performed on these specimens using XRD measurements covering a wide area of ~ 4 mm^2 surface area. Developments in grain misori-
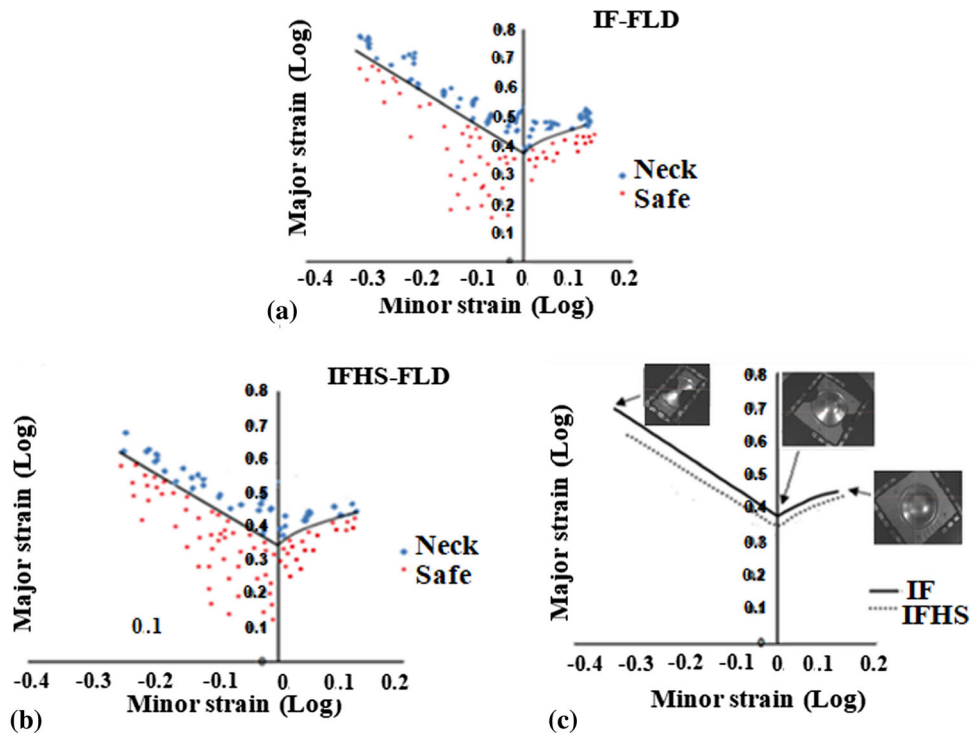
Fig. 4 Experimental forming limit diagrams: (a) IF steel, (b) IFHS steel and (c) IF and IFHS FLDs superimposed

Table 3 Effective strains (estimated after LDH experiments from Eq 2 using optical strain measurement system) for microstructural characterization of IF and IF-HS steels at various strains and strain paths

Strain path	Material	Low strain (LS)	Intermediate strain (IS)	High strain (HS)
Uniaxial strain(US)	IF	0.12	0.23	0.34
	IF-HS	0.12	0.24	0.35
Plane strain(PS)	IF	0.12	0.24	0.34
	IF-HS	0.13	0.25	0.34
Biaxial strain(BS)	IF	0.13	0.25	0.36
	IF-HS	0.12	0.25	0.35

entations were investigated by EBSD studies. The former was carried out on a PANAlytical, Netherlands XPert PRO MRD XRD machine and the latter was performed on a FEI™ Quanta 3D field emission gun (FEG) system. For EBSD measurements, 0.3 μm step size and similar beam and video conditions were maintained between different scans. Data above 0.1 confidence index (CI), a statistical measure of relative accuracy of indexing of Kikuchi patterns (Ref 33) were used for analysis. Data above 0.1 CI represent ~95% accuracy of indexing. The EBSD data were post processed to estimate GAM (grain average misorientation), which indicates average point-to-point misorientaion in a grain. A grain was denoted by the presence of >5° continuous boundary. The respective orientation distribution functions (ODFs) were determined using MTM-FHM software (Ref 34) by inversion of 4 incomplete pole figures and referring series expansion method (Ref 35). These are referred as functions on the orientation space that associates to each orientation ' g ' the volume percentage of crystals in a polycrystalline materials that are in this specific orientation. Standard φ_2 = 45° ODF section was used for indicating texture (Ref 36-38). Maximum ODF intensity as well as texture index (TI) (equation (3)) was also estimated from respective ODFs.

$$\text{TI} = \int f(g)^2 dg \qquad \text{(Eq 3)}$$

where $f(g)$ is the orientation density in terms of times random and ' dg ' is the Gaussian spread. In order to compare x-ray measured texture, TI has been considered (Ref 39-41) to be better than the conventional maximum ODF intensity ($f(g)$ maximum) values. Finally, the texture estimated normal anisotropy values for the chosen specimens were estimated (Ref 39) from the orientation distribution functions using Taylor theory (Ref 42).

(a)

IF-HS steel

Specimen width 25 mm

Specimen width 125 mm   Specimen width 200 mm
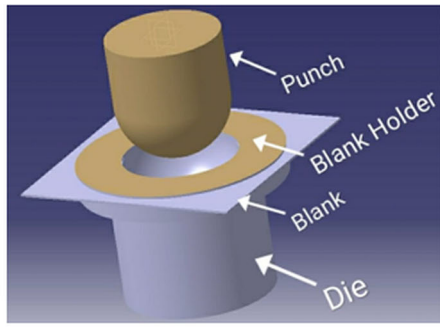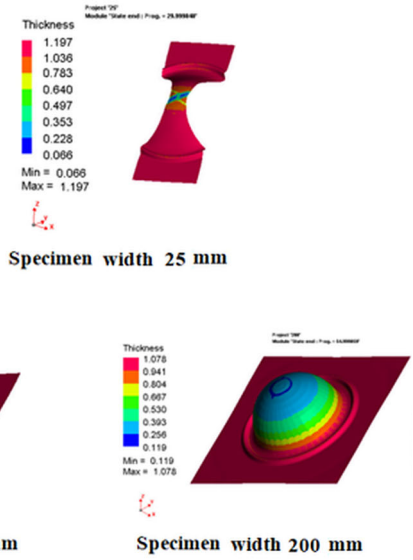
(b)

Fig. 5 Thickness in different width specimen during finite element (FE) simulated forming limit diagrams for IF-HS steel sheets
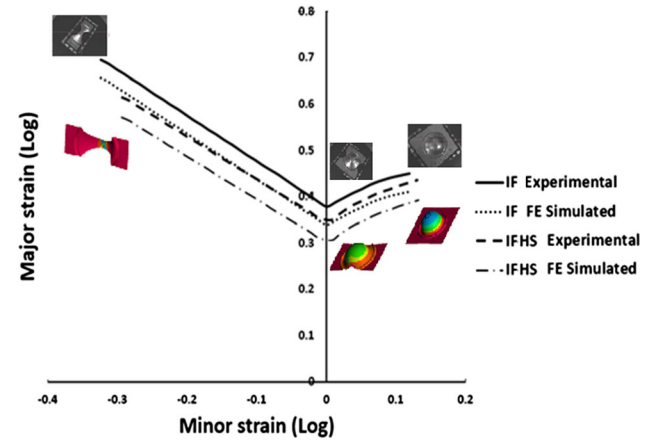

Fig. 6 Experimental and FE simulated forming limit diagrams for (a) IF and (b) IFHS grade steel sheets. (Constant and variable properties were included.)
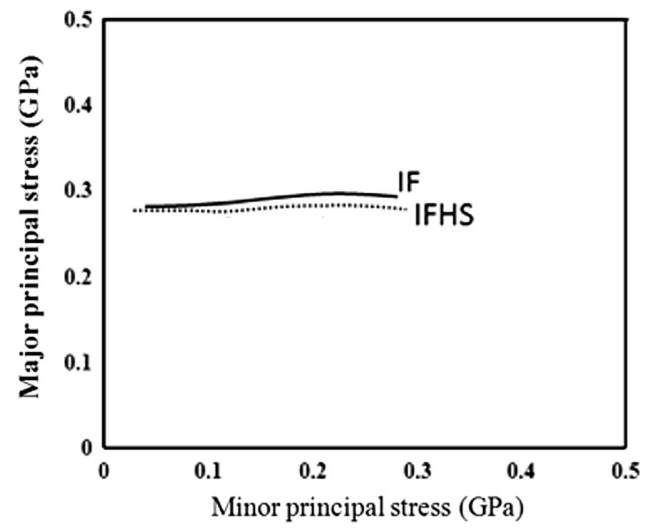

Fig. 7 Stress-based FLDs for IF and IFHS steel sheets

4. Forming Limit Diagram Predictions

A commercially available PAMSTAMP^{TM} software was used to determine finite element simulated FLDs for IF and IF-HS sheets. CAD models of tool setup and blanks were generated with CAD package SolidWorks. The surfaces of the tool parts were discretized by the triangle and quadrangle surface elements, assumed to be perfectly rigid. The blank sheet was discretized by four-node quadrilateral Belytschko–Tsay (BT) shell elements, representing the material with an elastic-plastic constitutive law. The blank was treated as deformable. Figure 5a shows computer-aided design (CAD) model of LDH test geometry. The material plasticity law of Hill's quadratic anisotropy function was assumed to be the yield criterion (32) as given in Eq 3.

where σ_{ij} indicates the stress values and F,G,H,L,M and N are the material constants which are described in terms of six yield stress ratios R_{11}, R_{22}, R_{33}, R_{12}, R_{13} and R_{23} as given in Eq (5-10)

$$F = \frac{1}{2}\left(\frac{1}{R_{22}^2} + \frac{1}{R_{33}^2} - \frac{1}{R_{11}^2}\right) \qquad \text{(Eq 5)}$$

$$F = \frac{1}{2}\left(\frac{1}{R_{33}^2} + \frac{1}{R_{11}^2} - \frac{1}{R_{22}^2}\right) \qquad \text{(Eq 6)}$$

$$f(\sigma) = \sqrt{F\,(\sigma_{22} - \sigma_{33})^2 + G(\sigma_{33} - \sigma_{11})^2 + H(\sigma_{11} - \sigma_{22})^2 + 2L\sigma_{23}^2 + 2M\sigma_{31}^2 + 2N\sigma_{12}^2} \qquad \text{(Eq 4)}$$

	Standard ODF	Rotated cube {001}<110> Cube {100}<001> θ-fiber {113}<110> I {112}<110> α-fiber E {111}<110> E' (111)<110> F' (111)<112> (554)<225> F (111)<112> γ-fiber Rotated Goss {100}<110> Goss {100}<001> φ₂= 45° constant

	IF	**IFHS**
Undeformed	PHI2= 45 Maximum ODF Intensity = 16.48 Texture Index = 7.115	PHI2= 45 Maximum ODF Intensity = 10.31 Texture Index = 4.059
Uniaxial Strain (US)	PHI2= 45 Maximum ODF Intensity = 11.68 Texture Index = 4.482	PHI2= 45 Maximum ODF Intensity = 9.29 Texture Index = 3.715
Plane Strain (PS)	PHI2= 45 Maximum ODF Intensity = 18.48 Texture Index = 7.867	PHI2= 45 Maximum ODF Intensity = 14.72 Texture Index = 5.579
Biaxial Strain (BS)	PHI2= 45 Maximum ODF Intensity = 25.23 Texture Index = 10.386	PHI2= 45 Maximum ODF Intensity = 21.58 Texture Index = 7.373

Fig. 8 φ_2=45° section of x-ray ODFs for samples subjected to different strain and strain modes (see Table 3). The prior deformation ODF and reference sections of bcc ideal orientations are included. Contour levels should be inserted. Contours: 1, 5, 15, 25, 35

$$F = \frac{1}{2}\left(\frac{1}{R_{11}^2} + \frac{1}{R_{22}^2} - \frac{1}{R_{33}^2}\right) \qquad \text{(Eq 7)}$$

$$L = 3/(2R_{23}^2) \qquad \text{(Eq 8)}$$

$$L = \frac{3}{2R_{31}^2} \qquad \text{(Eq 9)}$$

$$N = \frac{3}{2R_{12}^2} \qquad \text{(Eq 10)}$$

The yield stress ratios are expressed as a function of plastic anisotropy ratio as indicated in Eqs. (11-14):

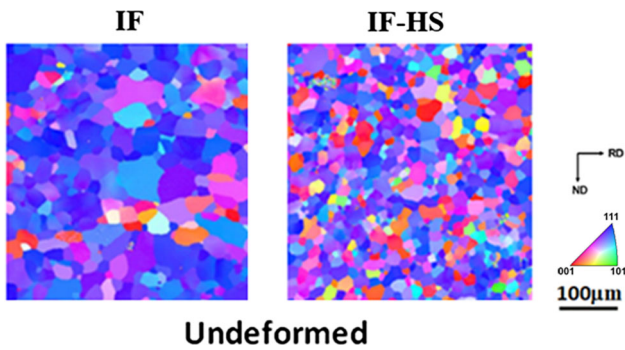$$R_{11} = R_{13} = R_{23} = 1 \qquad \text{(Eq 11)}$$

Fig. 9 EBSD IPF maps of IF and IFHS steel for undeformed samples (as received)
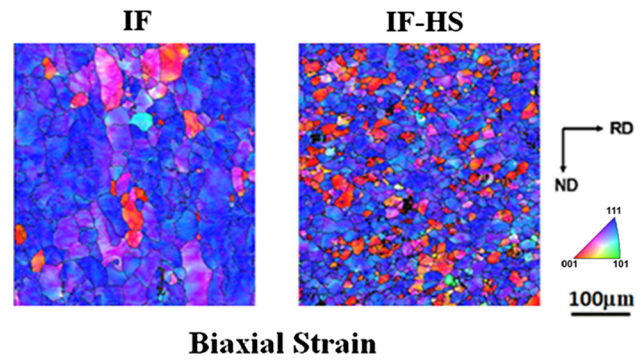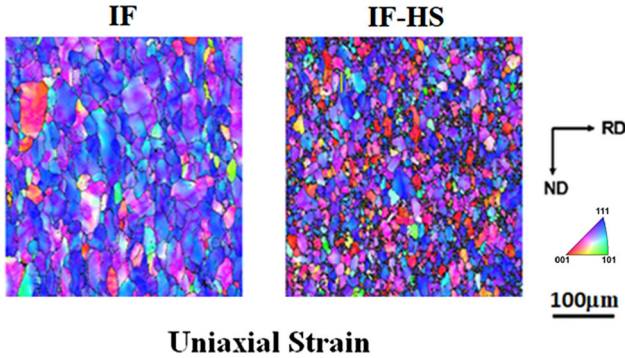

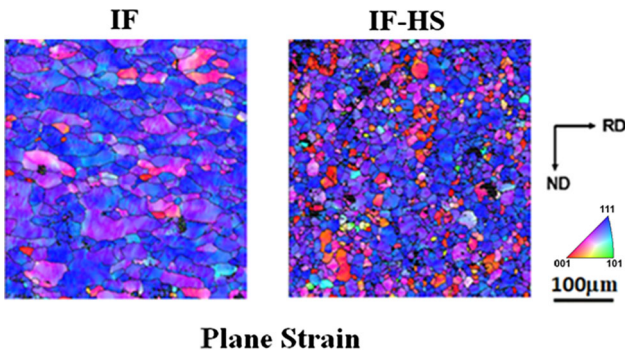**Fig. 10** EBSD IPF maps of IF and IFHS steel for uniaxial strain (US) path

Fig. 11 EBSD IPF maps of IF and IFHS steel for plane strain (PS) path

$$R_{22} = \sqrt{\frac{r_{90}(r_0 + 1)}{r_0(r_{90} + 1)}} \quad \text{(Eq 12)}$$

$$R_{33} = \sqrt{\frac{r_{90}(r_0 + 1)}{r_0 + r_{90}}} \quad \text{(Eq 13)}$$

Fig. 12 EBSD IPF maps of IF and IFHS steel for biaxial strain (BS) path

$$R_{12} = \sqrt{\frac{3r_{90}(r_0 + 1)}{(2r_{45} + 1) + (r_0 + r_{90})}} \quad \text{(Eq 14)}$$

Coefficient of friction (μ) values between different tools were incorporated in FE simulations, identical to experimental values as given in (Ref 43, 44). For the material hardening behavior, the Holloman law ($\sigma = k\varepsilon^n$) was considered. For failure criterion, thickness gradient criterion was referred (Ref 25). From FE simulations, the thickness values at the region of necking were noted in all specimens. Figure 5b shows thickness in different width specimens during finite element (FE) analysis for IF-HS steel case. The elements were so picked at the failure zones such that failure criterion needs to be satisfied and respective major strains and minor strains were noted. From these strain values, respective FLDs were predicted. The superimposed experimental and FE simulated FLDs are represented in Fig. 6. The stress-based FLDs, however, are widely known as strain path independent at different strain levels (Ref 45). Stress-based FLDs determined for both steels are shown in Fig. 7. These were constructed by plotting the minor and major stresses determined on exactly the same elements considered during strain-based FE simulated FLDs. This method was repeated for all specimens and the FLDs were determined for IF and IF-HS steels.

5. Results and Discussion

5.1 FLDs of IF and IF-HS Steels

The forming limit diagrams determined using LDH tests for IF and IF-HS steels are indicated in Fig. 4 (a–c). FE simulated forming limit diagrams and stress-based forming limit diagrams for both steels are shown in Fig. 6 and 7, respectively. Higher limiting strains were observed in IF specimen than IF-HS specimen clearly exhibiting higher formability for IF material. This is due to the higher values of 'n' and $\bar{r}$ (see Table 2) for IF rather than IF-HS specimen. The variation in numerical values of 'n' and $\bar{r}$ could be possibly due to the varying texture and anisotropy evolution between the two steel sheets during deep drawing at different strains and strain modes. In IF steels, Ti and/or Nb are added to bind the solute carbon and nitrogen to
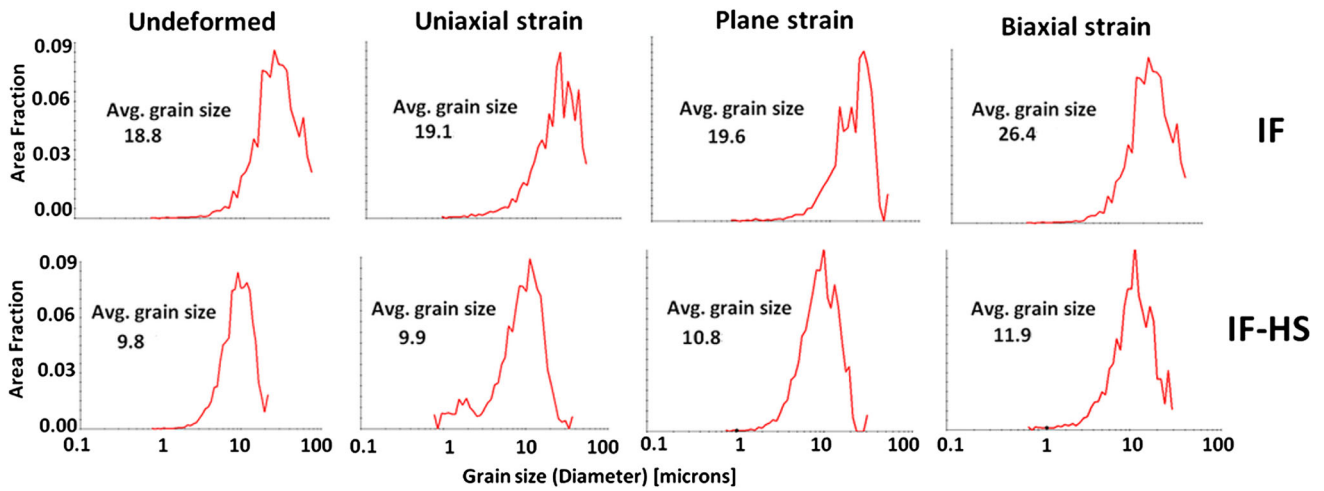
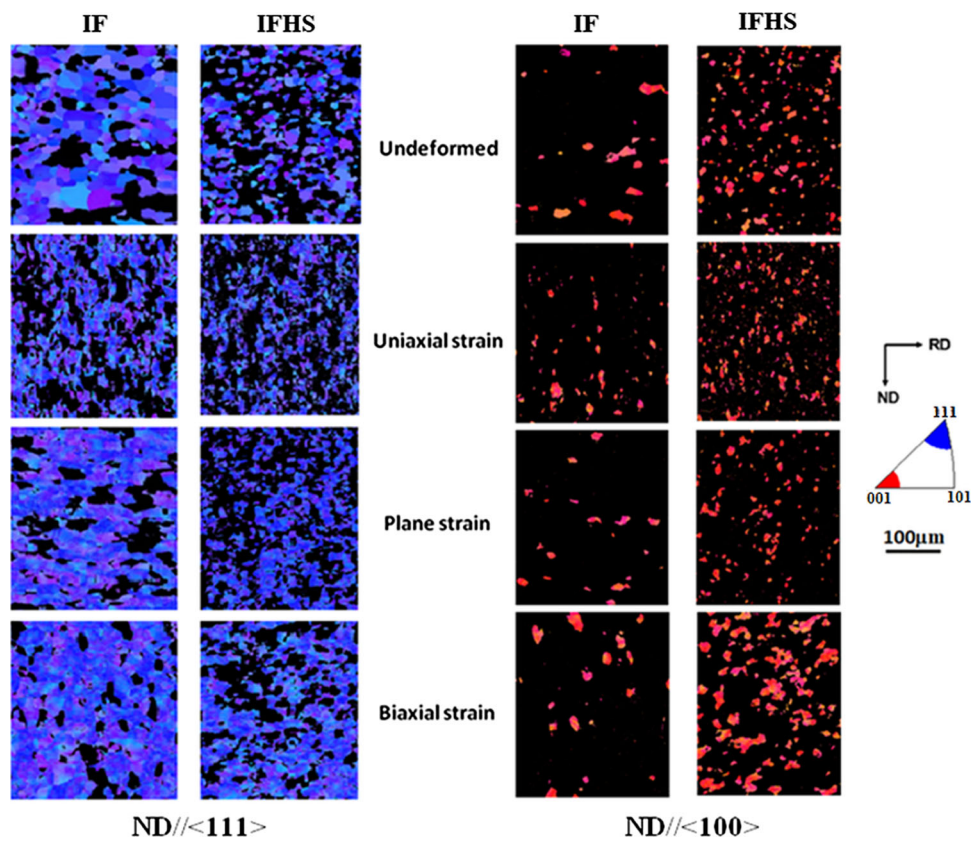**Fig. 13** Grain size distribution of IF and IFHS steel for undeformed and three more strain paths

Fig. 14 EBSD maps showing gamma (ND//<111>) and theta (ND//<100>) fibers of IF and IFHS steels for undeformed and three more strain paths

get carbides, nitrides and/or carbo-nitrides. These steels are therefore nearly free of solute atoms. It has been reported (Ref 37, 46) that increase in $\bar{r}$ value of the steel is due to reduction in solute carbon and nitrogen. However, such steels have very low yield strength. To overcome this problem, elements of solid solution strengthening like Mn, Si and P are usually added (as in IF-HS steels) or bake hardening phenomenon is used (as in BH steels). It has been reported that 'P' is the most economical and potent solid solution strengthening element, without appreciably affecting the deep drawing properties (Ref 37, 47) or in other words formability. IF steel also had higher work hardening rate (n value) than IF-HS steel.
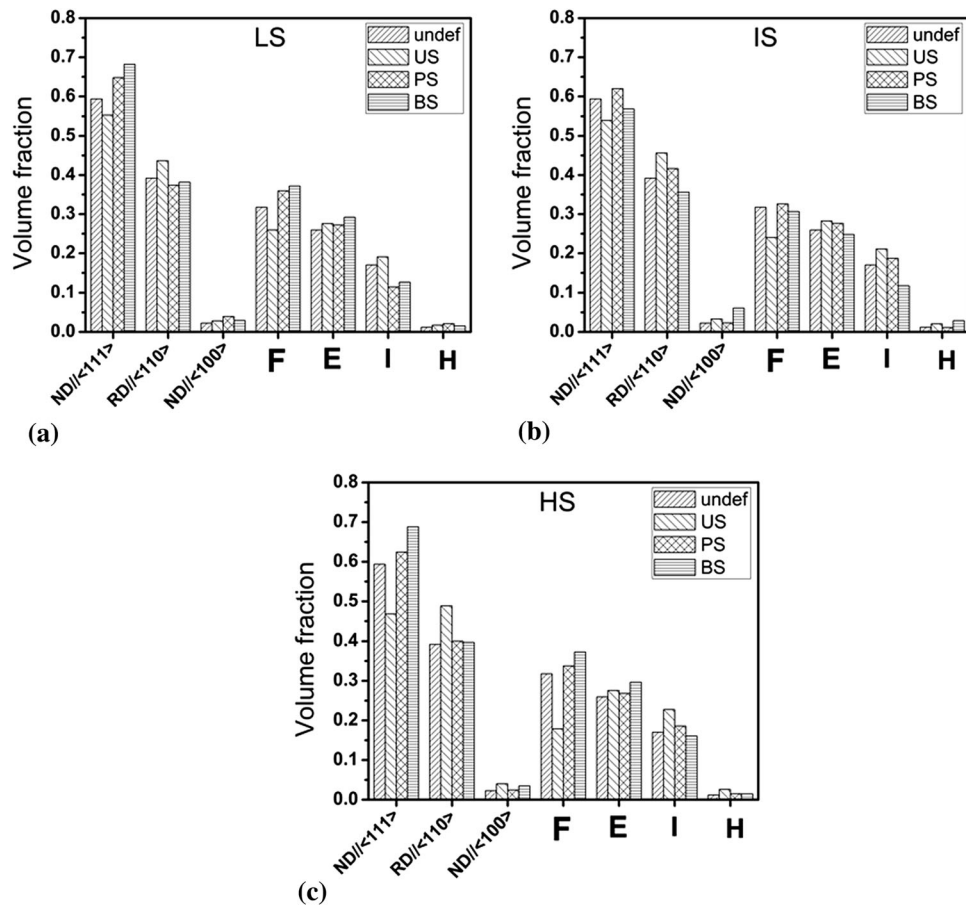
Fig. 15 Volume fraction of different fibers/texture components of IF steel for different strain paths and strains

6. Estimation of Microstructure and Texture Developments

Figure 8 shows the developments in texture (represented as ODFs) for various strain paths (US, PS and BS) and strains (LS, IS and HS) during FLD determination, i.e., plastic deformation. The relative anisotropy or extent of texturing is indicated by the texture index (TI) (Ref 41-43). The average plastic anisotropy index $\bar{r}$ can be estimated (Ref 27, 48) from the x-ray ODFs by using the Taylor theory (Ref 42). Earlier investigations showed that experimentally estimated $\bar{r}$ in x-ray peak profiles varies linearly with the intensities ratio of (111) and (100) (Ref 49). Formability of the material (often represented by $\bar{r}$) depends on grain size of the material and presence of crystallographic texture. A larger grain size and strong γ-fiber recrystallization texture are always treated desirable parameters for enhanced formability of LC steels. Cold rolling and recrystallization schedule are designed in such a way that a strong γ-fiber is obtained (Ref 37, 46). The ODFs in Fig. 8 indicate the formation of rotated cube (H) component for all the strain paths in case of IF-HS steel and not in IF steel. It is reported that the reason for lower formability and failure of IF-HS steel is the formation of detrimental rotated cube texture component at lowest strain (LS) and its persistence till highest strain (HS).

This is an interesting observation and is not reported earlier for IF-HS steels during the determination of FLD. It has also been reported that during fracture, θ-fiber orientations are the orientation through which crack propagates in a brittle manner leading to abrupt failure.

Advancing these results, further EBSD investigations were studied on inverse pole figure (IPF) maps and the same are indicated for IF and IF-HS steels for undeformed, i.e., as received samples (Fig. 9) along with US (Fig. 10), PS (Fig. 11) and BS (Fig. 12) representing different strain paths. The θ-fiber grains, which are seen in red color in the ND IPF maps (Fig. 11, 12 and 13), are always higher in IF-HS steel than IF steel. In a conventional 2θ XRD scan, ratio of intensity of (222 or 111) peak profile to intensity of (200 or 100) peak profile scales with the volume fraction of desirable γ-fiber and undesirable θ-fiber and hence with the $\bar{r}$ (Ref 38, 39). Further, the grain size of IF steel was also always higher than the IF-HS steel for all the conditions of strain and strain path. Higher grain size also results in enhanced formability. The grain size distribution of IF and IFHS steels for undeformed and in three different strain paths are shown in Fig. 13. The initial average grain size of IF steel was almost 4-5 times that of IFHS steel. Smaller grain size results in enhanced strength and hence reduction in formability in general. It is clearly seen that the fraction of detrimental θ-
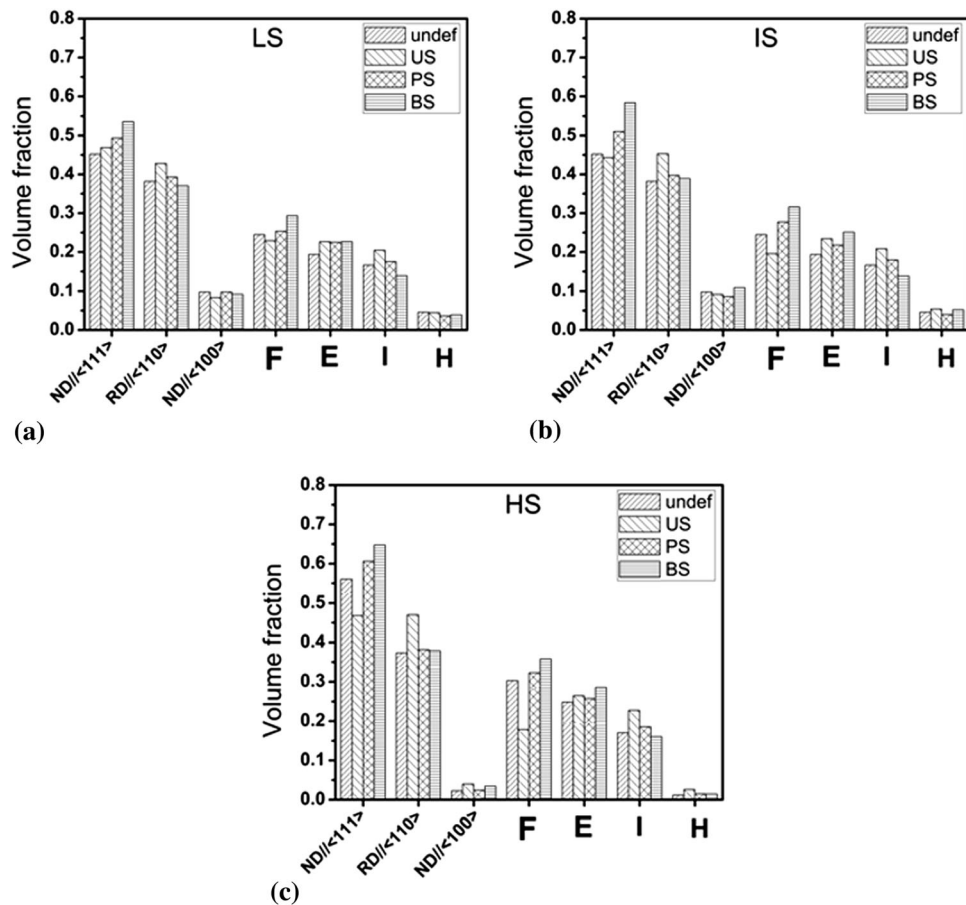
Fig. 16 Volume fraction of different fibers/texture components of IF-HS steel for different strain paths and strains

fiber was significantly larger in the IF-HS steel samples for all strains and strain paths than in IF steel. The partitioned EBSD maps of gamma (ND//<111>) and theta (ND//<100>) fibers of IF and IFHS steels for undeformed and three strain paths are shown in Fig. 14. The initial texture of the sheet is also important for enhanced formability in low carbon (LC) steels presence of strong γ-fiber recrystallization texture and corresponding absence of θ-fiber (Ref 38, 39, 46). Reduction in carbon enhances γ-fiber recrystallization formation, texture and hence improves formability. IF-HS specimen showed the presence of rotated cube ({100}<110>, a part of the θ-fiber) component in the texture of undeformed sample, which is considered to be a detrimental factor in its forming behavior. The volume fractions of these are quantified using x-ray texture (since it gives better statistics than EBSD measurements) and are shown in Fig. 15 and 16. F and E components are part of γ-fiber, while I and H are part of α-fiber (RD//110) and H is a part of θ-fiber. H is clearly higher in IF-HS steel for all conditions. All these clearly indicate that the presence of strong γ-fiber in initial sheet, large grain size and persistence of γ-fiber at all strains and strain paths during the determination of FLD is the reason for enhanced formability of IF steel than IF-HS steel. From EBSD data, the misorientation development in the form of kernel average misorientation (KAM) was also estimated for all conditions as shown in Fig. 17, confirming our observations of enhanced formability for IF steel.

7. Conclusions

The results clearly revealed that the microstructural developments at various strains and strain paths investigated have a significant influence on forming limit diagrams of IF and IF-HS steels. The findings of this work could potentially influence studies on effect of evolving microstructure during sheet metal forming. Key conclusions made are:

- IF steel had a higher plastic anisotropy ($\bar{r}$) and work hardening exponent (n) than IF-HS steel.
- Microstructure and texture developments were strain path dependent.
- The persistence of γ-fiber at all strains and strain paths is the driving factor for enhanced formability of IF steel.
- The pronounced θ-fiber development and presence of rotated cube texture component hindered formability in IF-HS steel significantly.
- Formability enhancing fibers/texture components quantified in terms of volume fraction were higher in case of IF steel, indicating that the steel is more formable.
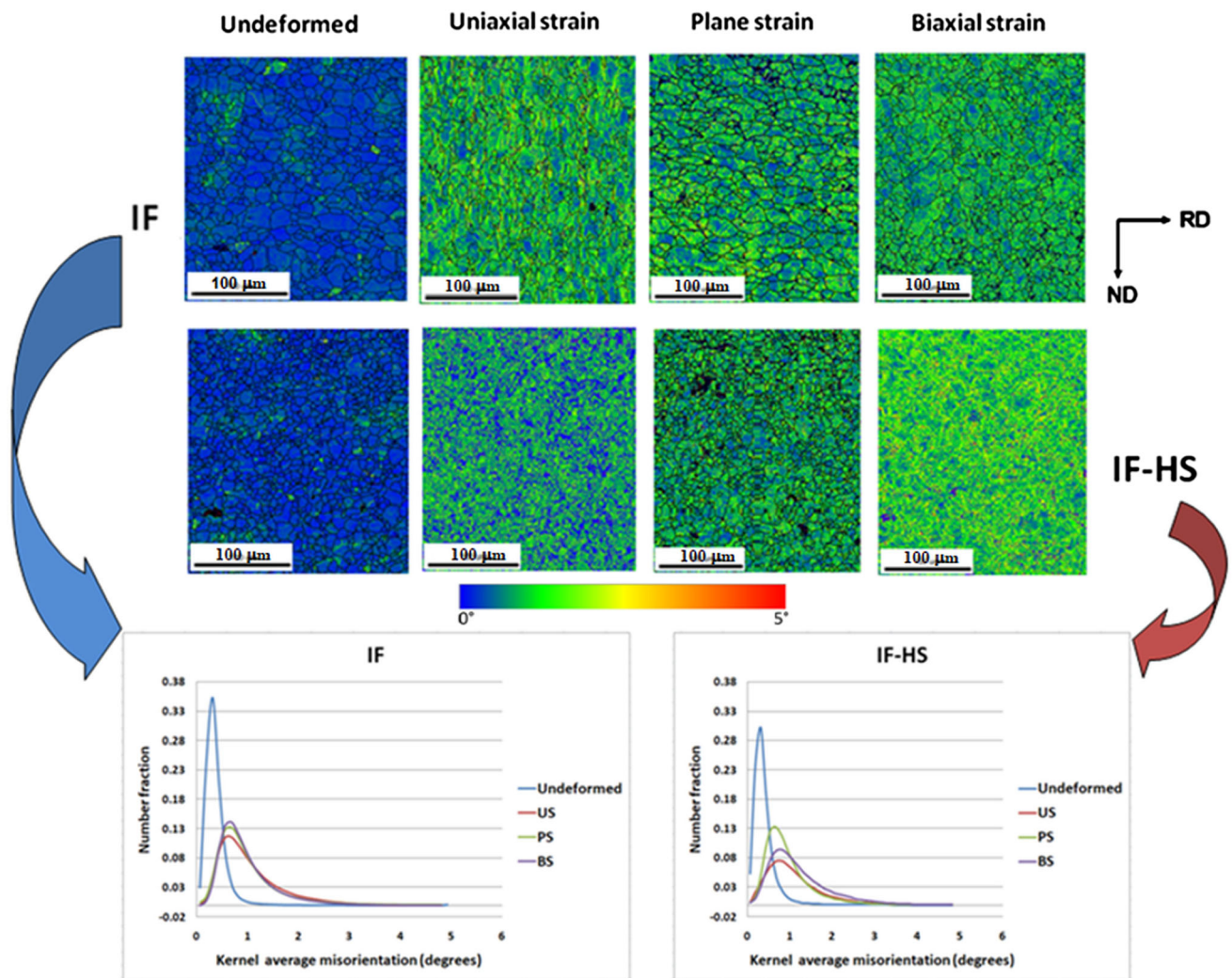
Fig. 17 EBSD-kernel average misorientaion (KAM) plots of IF and IFHS steel for undeformed, uniaxial strain (US), plane strain (PS) and biaxial strain (BS) path conditions

Conflict of interest

The authors declare that there is no conflict of interest.

References

1. G.M. Goodwin, Application of Strain Analysis to Sheet Metal Forming Problems in Press Shop, *Trans. SAE Paper*, 1968, **680093**, p 77–92
2. S.P. Keeler, Determination of Forming Limits in Automotive Stampings, *Sheet Metal Ind.*, 1965, **42**, p 683–695
3. S.P. Keeler and W.A. Backofen, Plastic Instability and Fracture in Sheets Stretched over Rigid Punches, *Trans. ASM*, 1946, **56**, p 30–48
4. J. Gronostajski and A. Dolny, Determination of Forming Limit Curves by Means of Marciniak Punch, *Memor. Sci. Rev. Metal.*, 1980, **4**, p 570–578
5. K.S. Raghavan, A Simple Technique to Generate in-Plane Forming Limit Curves and Selected Application, *Metall. Trans. A*, 1995, **26**, p 2075–2084
6. P. Vacher, A. Haddad and R. Arrieux, Determination of the Forming Limit Diagrams Using Image Analysis by the Correlation Method, *CIRP Ann. Manuf. Technol.*, 1999, **48**(1), p 227–230
7. ISO 12004-2:2008. Metallic Materials—Sheet and Strip—Determination of Forming Limit Curves—Part 2: Determination of Forming Limit Curves in the Laboratory, (2008)
8. Z.H. Lu and D. Lee, Prediction of History-Dependent Forming Limits by Applying Different Hardening Models, *Int. J. Mech. Sci.*, 1987, **29**, p 123–137
9. T. Yoshida, T. Kayayama and M. Usuda, Forming-Limit Analysis of Hemispherical-Punch Stretching Using the three-Dimensional Finite-Element Method, *J. Mat. Proc. Tech.*, 1995, **50**, p 226–237
10. E. Nakamachi, Sheet-Forming Process Characterization Bystatic-explicit Anisotropic Elastic-Plastic Finite-Element Simulation, *J. Mat. Proc. Tech.*, 1995, **50**, p 116–132
11. H. Takuda, K. Mori, N. Takakura and K. Yamaguchi, Finite Element Analysis of Limit Strains in Biaxial Stretching of Sheet Metals Allowing for Ductile Fracture, *Int. J. Mech. Sci.*, 2000, **42**, p 785–798
12. R.D. McGinty and D.L. McDowell, Application of Multiscale Crystal Plasticity Models to Forming Limit Diagrams, *J. Eng. Mater. Technol.*, 2004, **126**, p 285–291

13. H.B. Campos, M.C. Butuc, J.J. Grácio, J.E. Rocha and J.M.F. Duarte, Theoretical and Experimental Determination of the Forming Limit Diagram for the AISI 304 Stainless Steel, *J. Mater. Process. Technol.*, 2006, **179**, p 56–60

14. H. Aretz, Numerical Analysis of Diffuse and Localized Necking in Orthotropic Sheet Metals, *Int. J. Plast.*, 2007, **23**, p 798–840

15. M. Ganjiani and A. Assempour, An Improved Analytical Approach for Determination of Forming Limit Diagrams Considering the Effects of Yield Functions, *J. Mater. Process. Technol.*, 2007, **182**, p 598–607

16. J.W. Signorelli, M.A. Bertinetti and P.A. Turner, Predictions of Forming Limit Diagrams Using a Rate-Dependent Polycrystal Self-consistent Plasticity Model, *Int. J. Plast.*, 2009, **25**, p 1–25

17. P. Hora, L. Tong, J. Reissner, A Prediction Method of Ductile Sheet Metal Failure in FE Simulation, Numisheet, Dearborn, Michigan, USA, (1996) 252–256

18. K. Mattiasson, M. Sigvant, M. Larson, Methods for Forming Limit Prediction in Ductile Metal Sheets, IDDRG, Porto, Portugal, (2006) 1–9

19. G. Franz, F. Abed-Meraim, T. Ben Zineb, X. Lemoine and M. Berveiller, Role of Intragranular Microstructure Development in the Macroscopic Behavior of Multiphase Steels in the Context of Changing Strain Paths, *Mater. Sci. Eng. A.*, 2009 https://doi.org/10.1016/j.msea.2009.03.074

20. G. Franz, F. Abed-Meraim, T. Ben Zineb, X. Lemoine and M. Berveiller, Strain Localization Analysis for Single Crystals and Polycrystals: Towards Microstructure-Ductility Linkage, *Int. J. Plast.*, 2013, **48**(1), p 1–33

21. G. Franz, T. Abed-Meraim, T. Balan and G. Altmeyer, Investigation and Comparative Analysis of Plastic Instability Criteria: Application to Forming Limit Diagrams, *Int J Adv Manuf Technol*, 2014, **71**, p 1247–1262

22. S.E. Clift, P. Hartly, C.E.N. Sturgess and G.W. Rowe, Fracture Prediction in Plastic Deformation Processes, *Int J Mech Sci*, 1990, **32**, p 1–17

23. F. Ozturk and D. Lee, Analysis of Forming Limits Using Ductile Fracture Criteria, *J. Mater. Process. Technol.*, 2004, **147**(3), p 397–404

24. H. Takuda, K. Mori and N. Hatta, The Application of Some Criteria for Ductile Fracture to the Prediction of the Forming Limit of Sheet Metals, *J. Mater. Process. Tech.*, 1999, **95**, p 116–121

25. V. M. Nandedkar, Formability Studies on Deep Drawing Quality Steel, PhD thesis, IITBomaby, Mumbai (2000)

26. W.M. Sing and K.P. Rao, Influence of Material Properties on Sheet Metal Formability Limits, *J Mater Process Technol*, 1993, **37**, p 37–51

27. S.K. Yerra, H.V. Vankudre, P.P. Date and I. Samajdar, Effect of Strain Path on the Formability of a Low Carbon Steel - on the Textural and Microtextural developments, *J. Eng. Mater. Tech.*, 2004, **126**(1), p 53–61

28. S. Raveendra, A.K. Kanjarla, H. Paranjape, S.K. Mishra, S. Mishra, L. Delannay, I. Samajdar and P. Van Houtte, Strain Mode Dependence of Deformation Texture Developments: Microstructural Origin, *Met. Trans. A*, 2011, **42A**, p 2113–2124

29. L.S. Toth, J. Hirsch and P. Van Houtte, On the Role of Texture Development in the Forming Limits of Sheet Metals, *Int. J. Mech. Sci.*, 1996, **38**, p 1117–1126

30. S.K. Mishra, G.D. Sharvari, P. Pant, K. Narasimhan and I. Samajdar, Improved Predictability of Forming Limit Curves Through Microstructural Inputs, *Intl. J. Metal. Form.*, 2009, **2**, p 59–67

31. S. Chakrabarty, M. Bhargava, H.K. Narula, P. Pant and S.K. Mishra, Prediction of Strain Path and Forming Limit Curve of AHSS by Incorporating Microstructure Evolution, *Int. J. Adv. Manu. Tech.*, 2020 https://doi.org/10.1007/s00170-020-04948-0

32. R. Hill, A Theory of Yielding and Plastic Flow of Anisotropic metals, *Proc. Roy. Soc. London A*, 1948, **193**, p 281–297

33. M.M. Nowell and S.I. Wright, Orientation Effects on Indexing of Electron Backscattered Diffraction Patterns, *Ultramicroscopy*, 2005, **103**, p 41–58

34. H.J. Bunge, *Texture Analysis in MaterialsScience*, Butterworths, London, 1982

35. R. Khatirkar, K.V. Mani Krishna, L.A.I. Kestens, R. Petrov, P. Pant and I. Samajdar, Strain Localizations in Ultra Low Carbon Steel: Exploring the Role of Dislocations, *ISIJ Intl*, 2011, **51**(5), p 849–856

36. B. Verlinden, J. Driver, I. Samajdar, R. D. Doherty, Thermo-Mechanical Processing of Metallic Materials, ISBN–978-0-08-044497-0, 2007; Pergamon Materials Series—series ed. R.W. Cahn, Elsevier, Amsterdam

37. R.K. Ray, J.J. Jonas and R.E. Hook, Cold Rolling and Annealing Textures in low Carbon and Extra Low Carbon Steels, *Int Mater Rev*, 1994, **39**(4), p 129–171

38. V.M. Nandedkar, I. Samajdar and K. Narashiman, Development of Grain Interior Strain Localizations during Plane Strain Deformation of a Deep Drawing Quality Steel, *ISIJ Int*, 2001, **41**(12), p 1517–1521

39. P. Van-Houtte, MTM-FHM Software System, version 2, MTM, KULeuven, Belgium (1995)

40. P. Van Houtte, S. Li, M. Seefeldt and L. Delannay, Deformation Texture Prediction: from the Taylor Modelto the Advanced Lamel Model, *Int. J. Plasticity*, 2005, **21**, p 589–624

41. L. Delannay, P.J. Jacques and S.R. Kalidindi, Finite Element Modeling of Crystal Plasticity with Grains Shaped as Truncated Octahedrons, *Int. J. Plasticity*, 2006, **22**, p 1879–1898

42. T. Gladman, *The Physical Metallurgy of Microalloyed Steels*, The Institute of Materials, London, 1997

43. W. Wang, R.H. Wagoner and X.J. Wang, Measurement of Friction Undersheet Forming Conditions, *Metal. Mat. Trans. A*, 1996, **27A**, p 3971–3981

44. D. Wilkund, B.G. Rosen and L. Gunnarsson, Frictional Mechanismsin Mixed Lubricated Regime in Steel Sheet Metal Forming, *Wear*, 2008, **264**, p 474–479

45. T.B. Stoughton and X. Zhu, Review of Theoretical Models of the Strain-Based FLD and Their Relevance to the Stress-Based FLD, *Int. J. Plast*, 2004, **20**, p 1463–1486

46. M. Hatherly, F.J. Humphreys, Recrystallization and Related Annealing Phenomena, Elsevier (2012)

47. W.B. Hutchinson, Development and Control of Annealing Textures in Low-Carbon Steels, *Int. Metals Reviews*, 1984, **29**, p 25–42

48. R.K.K. KhatirkarSunil, Comparison of Recrystallization Textures in Interstitial Free and Interstitial Free High Strength Steels, *Mater. Chem. Phys.*, 2011, **127**, p 128–136

49. Y. Hosoya, T. Urabe, K. Tahara, S. Kaneto, H. Ando and N.K.K. Technol, *Rev.*, 1995, **72**, p 1